SCIENCE CHINA
Chemistry

•ARTICLES•

August 2021 Vol.64 No.8: 1332–1339
https://doi.org/10.1007/s11426-021-1022-3

Conductive phthalocyanine-based metal-organic framework as a highly efficient electrocatalyst for carbon dioxide reduction reaction

Meng-Di Zhang[1,3,4†], Duan-Hui Si[1,4†], Jun-Dong Yi[1,2], Qi Yin[1], Yuan-Biao Huang[1,2,4*] & Rong Cao[1,2,4*]

[1]*State Key Laboratory of Structural Chemistry, Fujian Institute of Research on the Structure of Matter, Chinese Academy of Sciences, Fuzhou 350002, China;*
[2]*University of Chinese Academy of Sciences, Beijing 100049, China;*
[3]*College of Chemistry and Materials Science, Fujian Normal University, Fuzhou 350007, China;*
[4]*Fujian College, University of Chinese Academy of Sciences, Fuzhou 350002, China*

Received March 10, 2021; accepted May 8, 2021; published online July 20, 2021

Porous crystalline metal-organic frameworks (MOFs) are one class of promising electrode materials for CO_2 electroreduction reaction (CO_2RR) by virtue of their large CO_2 adsorption capacities and abundant tunable active sites, but their insulating nature usually leads to low current density. Herein, a two-dimensional (2D) Ni-phthalocyanine-based MOF (NiPc-Ni$(NH)_4$) constructed by 2,3,9,10,16,17,23,24-octaaminophthalocyaninato nickel(II) (NiPc-$(NH_2)_8$) and nickel(II) ions attained high electrical conductivity due to the high overlap of d-π conjugation orbitals between the nickel node and the Ni-phthalocyanine-substituted *o*-phenylenediamine. During CO_2RR, the NiPc-Ni$(NH)_4$ nanosheets achieved a high CO Faradaic efficiency of 96.4% at −0.7 V and a large CO partial current density of 24.8 mA cm^{-2} at −1.1 V, which surpassed all the reported two-dimensional MOF electrocatalysts evaluated in an H-cell. The control experiments and density functional theory (DFT) calculations suggested that the Ni-N_4 units of the phthalocyanine ring are the catalytic active sites. This work provides a new route to the design of highly efficient porous framework materials for the enhanced electrocatalysis *via* improving electrical conductivity.

metal-organic frameworks, electroreduction, conductive, CO_2, CO

Citation: Zhang MD, Si DH, Yi JD, Yin Q, Huang YB, Cao R. Conductive phthalocyanine-based metal-organic framework as a highly efficient electrocatalyst for carbon dioxide reduction reaction. *Sci China Chem*, 2021, 64: 1332–1339, https://doi.org/10.1007/s11426-021-1022-3

1 Introduction

Now, the high concentration of the greenhouse gas CO_2 in the atmosphere has caused environmental problems such as global warming and sea-level rise [1]. Thus, it is urgently desirable to reduce the CO_2 concentration to the normal level. The electrochemical conversion of CO_2 to valuable chemicals using renewable electricity is a promising alternative to realize carbon-energy balance and remit the environmental issues [2–5]. Among the electroreduction products, CO is considered as one of the important industrial feedstocks, which has been widely used for the Fischer-Tropsch synthesis to produce hydrocarbon liquid chemicals [6,7]. To date, various materials including noble metal-based materials (*e.g.*, Au, Ag, Pd) and single-atom catalysts (*e.g.*, Fe-N-C, Co-N-C, Ni-N-C) have been developed for CO_2RR to produce CO [8–13], but it still remains a challenge to

†These authors contributed equally to this work.
*Corresponding authors (email: ybhuang@fjirsm.ac.cn; rcao@fjirsm.ac.cn)

efficiently convert CO_2 with high current density. Thus, developing highly efficient electrocatalysts for CO_2RR to overcome these limitations is of paramount importance and urgency.

As we know, the homogeneous molecular catalysts such as metalophthalocyanines (MPcs, *e.g.*, M = Ni, Fe, Co) have been found to electroreduce CO_2 in an aqueous medium. However, the discrete metal complexes-based molecular electrocatalysts usually show poor activity with low selectivity and current density in comparison to those of Au, Ag, Cu-based inorganic solid electrodes [14,15]. Integration of high loading of electroactive metal complexes-based catalysts into porous conductive materials would be an effective strategy for CO_2RR to generate high current density. Porous crystalline metal-organic frameworks (MOFs) with periodically arranged metal ions/clusters and organic ligands are considered to be promising candidates for CO_2RR as their high surface areas, large CO_2 adsorption uptakes, and high density of tunable active single-sites [16–21]. However, most of the conventional MOFs constructed by carboxylate-based linkages are electrical insulators, which usually exhibit low current density [22–25]. Recent progress in successful synthesis of electrically conductive two-dimensional (2D) MOFs [26–28] has endowed them with highly efficient electrocatlytic performance in CO_2RR. Nevertheless, to the best of our knowledge, few conductive MOFs have been reported for the electrocatalytic CO_2 reduction and their activities still need to be improved [27,29,30].

Herein, Ni-phthalocyanines (NiPc) based building block, an active molecular CO_2-reduction site, was integrated into a porous intrinsically conductive 2D MOF NiPc-Ni$(NH)_4$ for the efficient CO_2RR towards the CO_2-to-CO conversion in aqueous medium. Notably, the conductive 2D MOF NiPc-Ni$(NH)_4$, in which the planar NiPc motifs were linked by the Ni$(NH)_4$ nodes, shows highly electrical conductivity of 2.39×10^{-4} S m^{-1} due to the high overlap of d-π conjugation orbitals between the nickel node and the planar Ni-phthalocyanine-substituted *o*-phenylenediamine. Due to the remarkable electron transfer ability and high density of accessible active single-sites, the obtained conductive NiPc-Ni$(NH)_4$ nanosheets showed outstanding catalytic performance towards CO_2RR with a high CO selectivity of 96.4% at the applied potential of −0.7 V *versus* the reversible hydrogen electrode (RHE, all potentials are with reference to the RHE) and a large CO current density of 24.8 mA cm^{-2} at the potential of −1.1 V, which is the highest in reported 2D MOFs investigated in an H-type electrolysis cell [22,23,30,31]. The control experiments combined with density functional theory (DFT) calculations revealed that the catalytic active sites are Ni-N_4 units in phthalocyanine ring, while the square planar Ni$(NH)_4$ nodes accelerate the proton/electron transport to the active sites, thus improving the reaction kinetics of NiPc-Ni$(NH)_4$ during the CO_2-to-CO conversion.

2 Experimental

2.1 Reagents and chemicals

All reagents and chemicals were acquired from commercial sources and used as received unless specially noted. Nickel (II) chloride hexahydrate ($NiCl_2\cdot6H_2O$, ≥98%), dimethyl sulfoxide (DMSO, ≥99.5%), ammonia solution ($NH_3\cdot H_2O$, 25%–28%) and isopropanol ($(CH_3)_2CHOH$, ≥99.7%) were purchased from Sinopharm Chemical Reagent Co., China. Nafion (5 wt%, Sigma-Aldrich), carbon paper (Toray) and 2,3,6,7,10,11-hexaaminotriphenylene hexahydrochloride (HATP·6HCl, >95%, Tensus Biotech) were purchased from the corresponding company. Ultrapure water (18.25 MΩ cm) was used in all experiments.

2.2 Synthesis of NiPc-Ni$(NH)_4$ nanosheets

A solution of 21 mg of $NiCl_2\cdot6H_2O$ (88.4 μmol) in 20 mL of degassed DMSO and 1 mL of concentrated aqueous ammonia was added to a solution of 30 mg of NiPc-$(NH_2)_8$ (43.4 μmol) in 20 mL of degassed DMSO. The mixture was gently stirred at 60 °C in air for 12 h. After cooling to room temperature, the solid was filtered, washed successively with DMSO, water, MeOH and acetone, and dried under vacuum, to give NiPc-Ni$(NH)_4$ as black powder.

The NiPc-Ni$(NH)_4$ obtained by the above method was added to ethanol, followed by high-frequency sonication for 1.5 h at room temperature (25 °C). After high-speed centrifugation (12,000 r min^{-1}) to remove thick-layered sheets, the supematant was collected to give NiPc-Ni$(NH)_4$ nanosheets.

2.3 Synthesis of $Ni_3(HITP)_2$

A solution of 6.6 mg of $NiCl_2\cdot6H_2O$ (28 μmol) in 5 mL of degassed water and 0.3 mL of concentrated aqueous ammonia was added to a solution of 10 mg of HATP·6HCl (19 μmol) in 5 mL of degassed water. The mixture was gently stirred at 65 °C in air for 2 h. After cooling to room temperature, the solid was isolated by centrifugation, washed successively with water and acetone, and dried under vacuum, to give $Ni_3(HITP)_2$ as black powder.

2.4 Electrochemical measurements

Electrochemical experiments were implemented in a standard three-electrode H-type electrolysis cell with two compartments separated by a proton-exchange membrane (Nafion-117). Each compartment contained 70 mL electrolyte (0.5 M $KHCO_3$ made from ultrapure water). The working electrode was fabricated by coating 80 μL catalyst ink into carbon fiber paper electrode with 1 cm×1 cm. The homogeneous ink was prepared using 5 mg of catalyst and

2.5 mg ketjenblack dispersed into 1 mL of isopropanol containing 40 μL Nafion solution (5 wt%). The Ag/AgCl electrode and Pt guaze were as the reference electrode and counter electrode, respectively. Before the CO_2 electrochemical reduction, the electrolyte in the cathodic compartment was purged with CO_2 gas (average rate of 30 mL min^{-1} at room temperature and ambient pressure) at least 30 min to achieve the CO_2-saturated solution (pH=7.3). The Linear sweep voltammetry (LSV) curves were conducted with a scan rate of 10 mV s^{-1} in CO_2-saturated 0.5 M $KHCO_3$ electrolyte. In the studies, all potentials were normalized with respect to the RHE. The gas phase composition was analyzed by gas chromatograph (GC) equipped with a thermal conductivity detector (TCD) and a flame ionization detector (FID) every 15 min. The liquid products were analyzed by quantitative ^{1}H nuclear magnetic resonance (NMR) using DMSO as an internal standard.

3 Results and discussion

3.1 Synthesis and characterization of electrocatalyst

As shown in Figure 1, the conductive 2D MOF NiPc-Ni(NH)$_4$ was synthesized by the reaction of 2,3,9,10,16,17,23,24-octaaminophthalocyaninato nickel(II) (NiPc-(NH$_2$)$_8$) (Scheme S1, Supporting Information online) and $NiCl_2 \cdot 6H_2O$ in DMSO in the presence of aqueous ammonia [28,32,33]. The powder X-ray diffraction (PXRD) pattern (Figure 2a) of NiPc-Ni(NH)$_4$ is in an agreement with the simulated slipped AA-stacking model with orthorhombic *Cmcm* space group where a=25.5 Å, b=25.7 Å, c=6.7 Å, and $\alpha=\beta=\gamma=90°$ that built by Materials Studio 7.0. The Rietveld refinements reproduced the experimentally detected PXRD pattern with reasonable differences (R_p, 2.77% and R_{wp}, 3.53%), which suggested the correctness of the slipped AA-stacking model. The PXRD pattern of NiPc-Ni(NH)$_4$ (Figure 2a) demonstrates its crystalline nature with two diffraction peaks at 4.9° and 9.9° indexed to the (110) and (220) facets of the square lattice, respectively. An additional peak at 26.4° ascribed to (002) facet reveals the layer stacking structure along the c axis. The space-filling structural model of NiPc-Ni(NH)$_4$ (Figure 1) shows 1D square channels with 1.78 nm, while running along the c direction with a distance of 0.34 nm between the stacking 2D conjugated layers. Therefore, the nitrogen atoms of the amino groups in NiPc-(NH$_2$)$_8$ ligands were successfully coordinated with Ni(II) ions in a square planar geometry, resulting in a fully π-conjugated 2D skeleton in NiPc-Ni(NH)$_4$. In addition, no obvious peak corresponding to Ni nanoparticles (NPs) was observed in the PXRD patterns (Figure S1, Supporting Information online), implying that the Ni ions were not reduced during the synthesis process and the Ni species were in highly dispersed form.

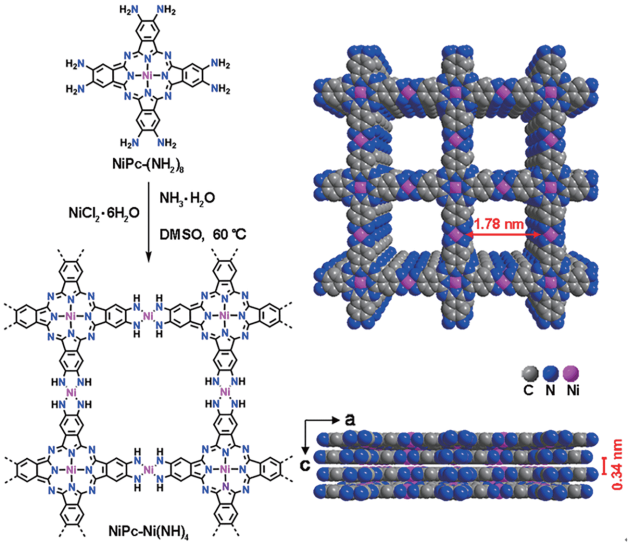

Figure 1 Synthetic scheme for 2D conductive NiPc-Ni(NH)$_4$. Top (right up) and side views (right bottom) of the structure of NiPc-Ni(NH)$_4$ with 2×2 square grids in slipped stacking mode. Hydrogen atoms are omitted for simplicity (color online).

To verify the formation of Ni(NH)$_4$ linkages in the NiPc-Ni(NH)$_4$, the Fourier transform infrared spectroscopy (FT-IR) measurements were conducted. As shown in Figure 2b, the ligand NiPc-(NH$_2$)$_8$ exhibits two strong absorption bands at 3,340 and 3,205 cm^{-1} originating from the N–H vibrations of the amino groups, which are not observed in the FT-IR of NiPc-Ni(NH)$_4$, indicating that the ligand NiPc-(NH$_2$)$_8$ was coordinated with nickel(II) ions. The scanning electron microscopy (SEM) images of NiPc-Ni(NH)$_4$ in Figure S2 provide visualization of a stacked layered morphology, which is also supported by the transmission electron microscopy (TEM) images (Figure 2c, d). Besides, no obvious Ni NPs were observed in the TEM and high-angle annular dark-field scanning transmission electron microscopy (HAADF-STEM) images (Figure 2c–e), which agrees well with the PXRD result. The energy-dispersive X-ray spectroscopy (EDS) elemental mapping images (Figure 2e) reveal well dispersed C, N and Ni elements, highlighting the advantage of the periodically arranged crystalline frameworks with single-sites. The inspection of survey spectrum in X-ray photoelectron spectroscopy (XPS) result (Figure S3a) further evidenced the presence of C, N, and Ni elements in NiPc-Ni(NH)$_4$, while the O element may originate from the coordinated water guest molecules [32], which was consistent with the thermogravimetric analysis (TGA) result (Figure S4). The high-resolution Ni 2p spectrum of NiPc-Ni(NH)$_4$ (Figure S3b) displays two dominated peaks centered at the binding energies of 855.5 eV (Ni 2p$_{3/2}$) and 872.9 eV (Ni 2p$_{1/2}$), indicating the Ni species in both of the NiPc ligand and Ni(NH)$_4$ node were mainly existed as Ni^{2+}. The satellite peaks located at higher energy sides of Ni 2p$_{3/2}$ and Ni 2p$_{1/2}$ levels are likely associated with the shakeup

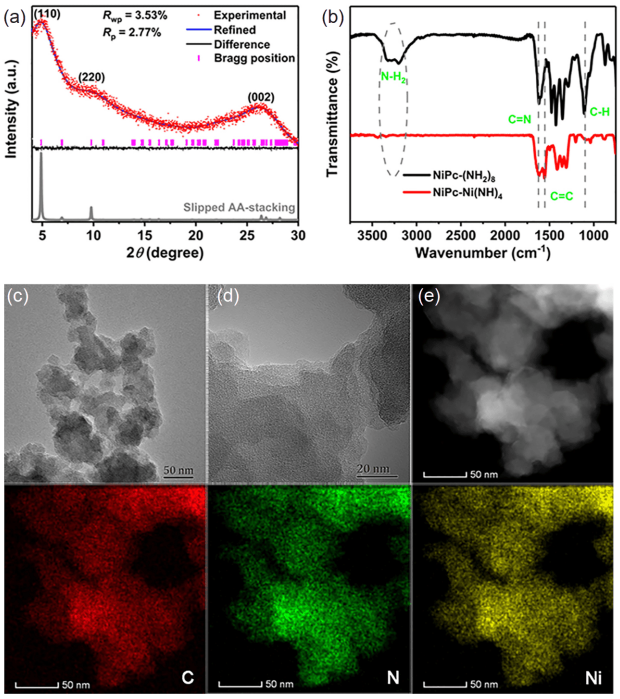

Figure 2 (a) Experimental (red dot), Rietveld-refineand (blue line) and simulated (slipped AA-stacking mode, grey line) PXRD patterns of NiPc-Ni(NH)$_4$. (b) FT-IR spectra of NiPc-(NH$_2$)$_8$ (black) and NiPc-Ni(NH)$_4$ (red). (c, d) TEM images of NiPc-Ni(NH)$_4$ with 50 and 20 nm scale-bar, respectively. (e) HAADF-STEM image of NiPc-Ni(NH)$_4$ and EDS mapping of C, N, and Ni elements (color online).

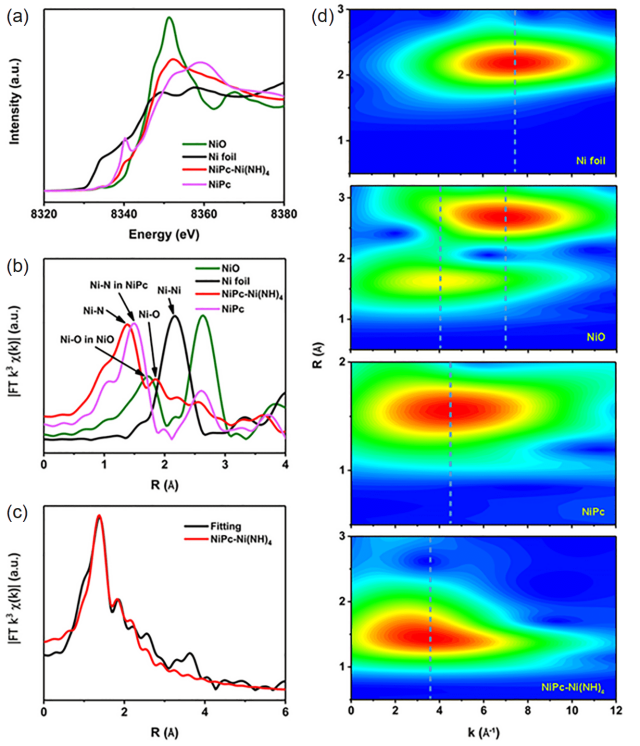

Figure 3 (a) Normalized Ni K-edge XANES spectra of the Ni foil, NiO, NiPc and NiPc-Ni(NH)$_4$; (b) Fourier transform EXAFS spectra of the Ni foil, NiO, NiPc and NiPc-Ni(NH)$_4$; (c) the corresponding EXAFS fitting curves of NiPc-Ni(NH)$_4$; (d) wavelet transform EXAFS spectra of the Ni foil, NiO, NiPc and NiPc-Ni(NH)$_4$ (color online).

excitation of Ni^{2+} [34,35]. The fitted N 1s spectra (Figure S3c) show the peaks of 398.8, 399.8 and 400.5 eV, which can be assigned to N–Ni, C–N=C of phthalocyanine ring and uncoordinated C–NH$_2$ at the defect and edge sites, respectively [32–34,36]. Inductively coupled plasma atomic emission spectroscopy (ICP-AES) revealed that the obtained NiPc-Ni(NH)$_4$ had a high Ni content of 17.18 wt%, suggesting high loading of NiPc active sites were integrated into the framework and would enable an efficient CO_2RR. Notably, the measured Ni content was slightly lower than the theoretical value of 22 wt%, which was mainly ascribed to the presence of unreacted –NH$_2$ groups at the edges of NiPc-Ni(NH)$_4$, as proved by the XPS result (Figure S3).

To further gain insight into the Ni coordination environment of NiPc-Ni(NH)$_4$, the Ni K-edge X-ray absorption near-edge structure (XANES) and extended X-ray absorption fine structure (EXAFS) spectra were performed. As shown by the XANES curves in Figure 3a, the Ni absorption edge energy position of NiPc-Ni(NH)$_4$ is very close to that of the NiO, which suggests the valence state of Ni atom as +2 in both of the NiPc ligand and Ni(NH)$_4$ node [30], in alignment with the XPS result. Moreover, a weak pre-edge peak at around 8334 eV for NiPc-Ni(NH)$_4$ is observed, which corresponds to the dipole-forbidden but quadrupole-allowed transition from 1s to 3d [7]. Meanwhile, NiPc-Ni(NH)$_4$ shows a strong absorption peak at about 8340 eV similar to the reference sample NiPc, which is associated with the 1s to 4p electronic transition [7]. The results suggested that the Ni atoms in NiPc-Ni(NH)$_4$ adopt similar coordination configuration to NiPc with Ni-N$_4$ structure [35]. The Fourier transform EXAFS (FT-EXAFS) spectrum of NiPc-Ni(NH)$_4$ (Figure 3b) clearly demonstrates an intense signal at 1.39 Å, which can be ascribed to the characteristic Ni-N coordination path. Notably, compared with the Ni-N coordination peak at 1.48 Å for the reference NiPc, the corresponding *R* value in NiPc-Ni(NH)$_4$ slightly shifts to 1.39, which can be attributed to the existence of shorter Ni–N bond of Ni(NH)$_4$ node in the framework of NiPc-Ni(NH)$_4$ [34,35]. The EXAFS spectrum of NiPc-Ni(NH)$_4$ also shows an obvious signal at 1.84 Å, near to the Ni-O position (1.74 Å) of NiO, which may be ascribed to the coordination of water molecules to Ni atom in the axial direction perpendicular to Ni-N$_4$ plane in NiPc-Ni(NH)$_4$. Furthermore, the peak at the position of Ni-Ni coordination was absent in the Ni K-edge EXAFS curve of NiPc-Ni(NH)$_4$, which manifested that no Ni particles existed in the NiPc-Ni(NH)$_4$ sample and the Ni species were in atomically isolated form. In addition, according to the fitting result based on the EXAFS curves in Figure 3c and Table S1 (Supporting Information online), the Ni species in NiPc-Ni(NH)$_4$ is coordinated with four nitrogen atoms and one

oxygen atom from the coordinated water molecule. Wavelet transform EXAFS (WT-EXAFS) is considered to be a good supplement for FT-EXAFS owing to its powerful resolution in both *k* and *R* spaces [37,38]. The WT contour plots of NiPc-Ni(NH)$_4$ (Figure 3d) show the intensity maximum at 3.6 Å^{-1}, which can be assigned to the Ni–N(O) contribution. The WT signals associated with the Ni–Ni bond were not detected, as compared with the WT contour plots of Ni foil and NiO standards. These further demonstrated that the Ni species are highly dispersed in NiPc-Ni(NH)$_4$, which is consistent with the aforementioned PXRD and TEM results.

The porous nature of NiPc-Ni(NH)$_4$ was further verified by the N_2 sorption isotherms at 77 K (Figure 4a), which revealed that it has a Brunauer-Emmett-Teller (BET) surface area of 172 m^2 g^{-1} (Table S2). The corresponding pore size distribution (Figure 4a inset) analyzed with the non-local density functional theory (NL-DFT) method showed that NiPc-Ni(NH)$_4$ has an accessible pore size of ~1.7 nm, which is consistent with simulated structure (Figure 1). Such large microporous structure would be beneficial for reactants diffusion and mass transport to improve the electrocatalytic activity. Moreover, the porous NiPc-Ni(NH)$_4$ has a large CO_2 adsorption capacity of 41 cm^3 g^{-1} at 298 K (Figure 4b), which suggests a strong CO_2 affinity by the NiPc-Ni(NH)$_4$ with a nitrogen-rich structure for enhancing its electrocatalytic activity in CO_2RR. In order to investigate the electrical conductivity capacity of NiPc-Ni(NH)$_4$, the conductivity measurement for the compressed NiPc-Ni(NH)$_4$ pellet with a thickness of 1.03 mm was performed with two-probe method [32]. As shown in Figure S5, NiPc-Ni(NH)$_4$ has a high electrical conductivity of up to 2.39×10^{-4} S m^{-1} at room temperature. The high conductivity value for NiPc-Ni(NH)$_4$ is several orders of magnitude higher than those of insulating MOFs [26], which would promote electronic transmission to the active sites and facilitate the energetic conversion efficiency. The Nyquist plots (Figure 4c) further confirm that the NiPc-Ni(NH)$_4$ sample has fast electron transport ability as verified by its small semicircular diameter at every potential in a wide potential range of −0.7 to −1.1 V (Table S3). To guarantee the well-defined Ni(II) active sites in the slipped AA-stacking frameworks are highly accessible to the reactive species and electrolytes during catalytic process, the NiPc-Ni(NH)$_4$ bulks were transformed into nanosheets by sonication exfoliation method [39,40]. The obtained NiPc-Ni(NH)$_4$ nanosheets were characterized by atomic force microscopy (AFM) (Figure 4d) and showed a uniform thickness of only 1.35 nm corresponding to four- to five-layer NiPc-Ni(NH)$_4$ nanosheets. Such an ultrathin 2D sheet structure would greatly enhance the specific surface area of NiPc-Ni(NH)$_4$ and contribute to the exposure of active centers to improve electrocatalysis.

3.2 Electrocatalytic performance for CO_2RR

The CO_2 electroreduction experiments were conducted in 0.5 M $KHCO_3$ aqueous electrolyte using a gas-tight H-type electrolysis cell separated by a proton-exchange membrane. As shown by the LSV curves in Figure 5a, NiPc-Ni(NH)$_4$ nanosheets showed a more positive onset potential and higher current density in CO_2-saturated 0.5 M $KHCO_3$ electrolyte relative to those in Ar-saturated corresponding electrolyte, suggesting its high CO_2 reactivity and the feasibility for CO_2RR. The gas chromatography (GC) and NMR analyses manifested that CO and H_2 are the only detectable gaseous products in the applied potential range from −0.7 to −1.1 V and no liquid product was formed in the CO_2RR

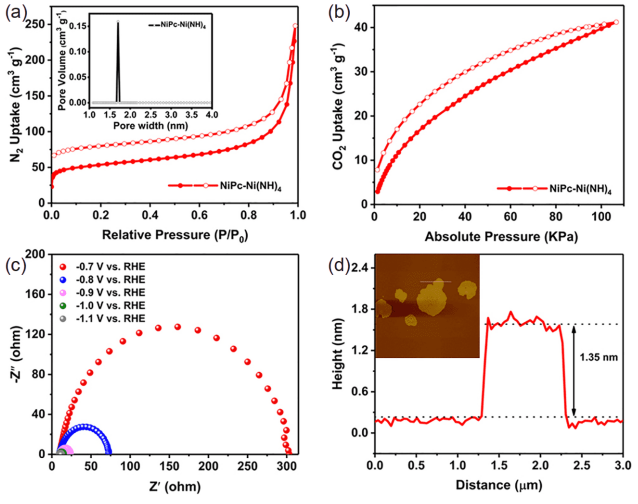

Figure 4 (a) N_2 sorption isotherms of NiPc-Ni(NH)$_4$ at 77 K (inset pore-size distribution profile); (b) CO_2 sorption isotherms of NiPc-Ni(NH)$_4$ measured at 298 K; (c) Nyquist plots from −0.7 to −1.1 V of NiPc-Ni(NH)$_4$; (d) AFM image (scale bar = 10 μm) and the corresponding cross-sectional profile of NiPc-Ni(NH)$_4$ nanosheets (color online).

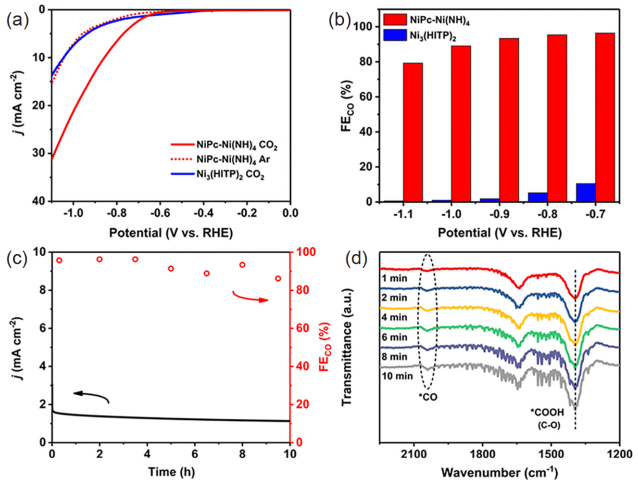

Figure 5 (a) LSV curves in the Ar-saturated and CO_2-saturated 0.5 M $KHCO_3$ electrolytes at a scan rate of 10 mV s^{-1}; (b) FE_{CO} from −0.7 to −1.1 V of NiPc-Ni(NH)$_4$ and $Ni_3(HITP)_2$; (c) stability test of NiPc-Ni(NH)$_4$ at −0.7 V for 10 h; (d) *operando* ATR-FTIR of NiPc-Ni(NH)$_4$ at −0.7 V in CO_2-saturated 0.5 M $KHCO_3$ electrolyte (color online).

(Figure S6). Notably, almost no CO was produced in the Ar-saturated 0.5 M $KHCO_3$ electrolyte (Figure S7), confirming that CO mainly originated from CO_2. As shown in Figure 5b, the NiPc-Ni$(NH)_4$ nanosheets exhibited impressive activity for the conversion of CO_2 to CO with over 89.1% Faradaic efficiency in a wide potential range of −0.7 to −1.0 V and achieved the highest CO faradaic efficiency (FE_{CO}) of 96.4% at −0.7 V. Meanwhile, the partial current density for CO (j_{CO}) of NiPc-Ni$(NH)_4$ nanosheets increased with more negative potentials applied, and reached a maximum value of 24.8 mA cm^{-2} at −1.1 V (Figure S8). Such excellent performance achieved by NiPc-Ni$(NH)_4$ nanosheets outperforms all the 2D MOF electrocatalysts (Figure S9) [22,23,30,31] and the vast majority of the 3D MOF electrocatalysts reported in H-type electrolysis cell (Table S4) [24,27,41–47]. This mainly results from their excellent electron conductivity and highly exposed active sites.

To evaluate the electrocatalytic stability of the NiPc-Ni$(NH)_4$ sample, a constant potential electrolysis of CO_2 was conducted (Figure 5c). At −0.7 V in CO_2-saturated 0.5 M $KHCO_3$ electrolyte, the catalyst attained a steady current density after half an hour and showed a Faradaic efficiency of 91%±5% for CO during 10 h electrolysis time, which demonstrated the good durability of the NiPc-Ni$(NH)_4$ catalyst. The TEM images (Figure S10a, b) of the NiPc-Ni$(NH)_4$ after electrolysis for 10 h confirmed that the catalyst can maintain its morphology during the CO_2RR. Furthermore, no Ni NPs were generated at NiPc-Ni$(NH)_4$ electrode under catalysis conditions. The PXRD profile of NiPc-Ni$(NH)_4$ after electrolysis (Figure S10c) revealed that the crystallinity of the catalyst remained almost unchanged when compared with that of the fresh catalyst. The oxidation state of Ni(II) was maintained, as verified by pre- and post-electrolysis analysis of NiPc-Ni$(NH)_4$ using XPS technique (Figure S10d). ICP result revealed that negligible leaching of nickel species was detected in the electrolyte (Table S5). All these results proved the good stability of NiPc-Ni$(NH)_4$ catalyst during CO_2RR.

3.3 Probing the active site for CO_2RR

To confirm whether the NiPc motif or Ni$(NH)_4$ node in NiPc-Ni$(NH)_4$ is the active site for CO_2RR, the typical conductive 2D MOF $Ni_3(HITP)_2$ containing the same Ni$(NH)_4$ nodes (Scheme S2) was also synthesized using 2,3,6,7,10,11-hexaaminotriphenylene hexahydrochloride and $NiCl_2{\cdot}6H_2O$ [28,32], as confirmed by PXRD pattern (Figure S11a), nitrogen sorption isotherms (Figure S11b and Table S2) and CO_2 sorption isotherms (Figure S11c). The impedance of $Ni_3(HITP)_2$ is similar to that of NiPc-Ni$(NH)_4$ at the same potential (Figure 4c and Figure S11d, Table S3), suggesting they have similar electron kinetics. The CO_2RR conditions for $Ni_3(HITP)_2$ were similar to that of NiPc-Ni$(NH)_4$. As shown by the LSV curves in Figure 5a, in CO_2-saturated electrolyte, NiPc-Ni$(NH)_4$ displayed more positive onset potential and much large current densities in comparison with $Ni_3(HITP)_2$, suggesting the key role of NiPc units for promoting CO_2RR. Furthermore, different from the NiPc-Ni$(NH)_4$ catalyst towards highly selective production of CO, H_2 was the major product for $Ni_3(HITP)_2$ over the investigated potential range (Figure 5b). Notably, the carbon fiber paper with ketjenblack and Nafion displayed almost no activity for CO_2RR and the H_2 yield are close to 100% (Figure S12). Moreover, no Ni NPs were observed in the TEM images (Figure S10a, b) of the NiPc-Ni$(NH)_4$ after CO_2RR for 10 h. Thus, it is reasonably believed that the NiPc units in NiPc-Ni$(NH)_4$ were the active centers for the electrocatalytic conversion of CO_2 to CO.

To further investigate the active site of NiPc-Ni$(NH)_4$ for CO_2RR, the theoretical calculations were further performed. As shown in Figure 6a, b, the CO_2RR pathway may consist of three reactions. First, *COOH was generated by an electron-proton coupling transfer process, which is considered to be the rate-determined step (RDS) and its free energy is 1.72 eV; Second, *COOH was converted to *CO through another electron-proton coupling transfer process; Finally, CO was desorbed and the free active site was regenerated. The HER pathway may consist of two reactions. The H was adsorbed to the active site and generated *H, which is identified as the rate-determined step and its free energy is 1.81 eV; Then, H_2 was desorbed to regenerate the free active site. It is obviously that the free energy for the RDS of CO_2RR (1.72 eV) is lower than that for HER (1.81 eV) by NiPc site of NiPc-Ni$(NH)_4$, which reinforced our experimental result that the CO_2RR occurred preferentially at NiPc site. The energies for CO_2RR and HER by Ni$(NH)_4$ site of NiPc-Ni$(NH)_4$ were also calculated as given in Figure S13. The free energy for the RDS of CO_2RR in Ni$(NH)_4$ is larger than that of HER, suggesting that the later reaction is dominated at Ni$(NH)_4$ site rather than CO_2RR. The above results were consistent with the experiments. The high ac-

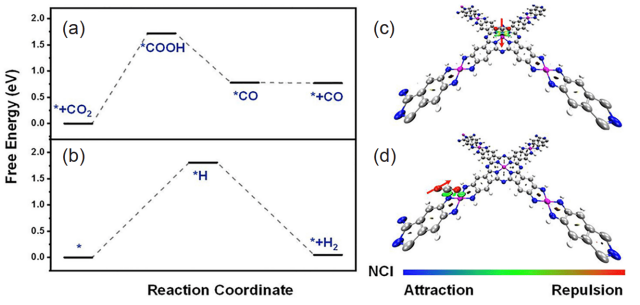

Figure 6 The calculated mechanisms of CO_2RR (a) and HER (b) by NiPc site of NiPc-Ni$(NH)_4$; (c) the noncovalent-interaction (NCI) between CO_2 molecule and NiPc site of NiPc-Ni$(NH)_4$; (d) the NCI between CO_2 molecule and Ni$(NH)_4$ site of NiPc-Ni$(NH)_4$ (The red arrow indicates the direction of atomic force) (color online).

tivity and selectivity of NiPc site in NiPc-Ni(NH)$_4$ for CO_2 RR were further explained in terms of noncovalent-interaction (NCI) and atomic force. As shown in Figure 6c, d, there is stronger van der Waals interaction between CO_2 molecule and NiPc site compared with Ni(NH)$_4$ site. Furthermore, the direction of CO_2 molecule force is from C atom of CO_2 molecule to Ni atom of NiPc site as the CO_2 adsorbed on NiPc site. In contrast, the direction of CO_2 molecule force is from O atom of CO_2 molecule to the centre of NiPc-Ni(NH)$_4$ fragment as the CO_2 adsorbed on Ni(NH)$_4$ site. It is clearly that the CO_2 molecule that adsorbed on Ni(NH)$_4$ site is easy to transfer to NiPc site. Thus, in this way, the CO_2RR active site can be determined as NiPc site of NiPc-Ni(NH)$_4$.

3.4 The reaction pathway of CO_2RR over NiPc-Ni(NH)$_4$

To explore possible reaction intermediates during CO_2RR and gain insights into the reaction pathway of CO_2RR over NiPc-Ni(NH)$_4$, *operando* electrochemical attenuated total reflectance Fourier transform infrared spectroscopy (ATR-FTIR) for NiPc-Ni(NH)$_4$ was recorded at −0.7 V in CO_2-saturated 0.5 M $KHCO_3$ electrolyte. As shown in Figure 5d, the strong peaks centered at 1,394 cm^{-1} can be seen clearly in these spectra, which consist of the C–O stretch of *COOH [48,49]. In addition, the weak peaks located at 2,042 cm^{-1} belonging to the *CO intermediate were observed [48]. And their intensity gradually increased with the formation of *COOH intermediate and finally reached dynamic balanced, which suggests that *CO should be derived from *COOH. Thus, the possible CO_2RR pathway of the conversion of CO_2 to CO on NiPc sites of NiPc-Ni(NH)$_4$ electrode is consistent with the above theoretical calculations results [50].

4 Conclusions

In conclusion, a conductive 2D NiPc-based MOF (NiPc-Ni(NH)$_4$), in which the square planar nickel(II) nodes were bridged by the octaamino-substituted nickel(II) phthalocyanine ligands, was constructed and employed as highly efficient electrocatalyst for CO_2 reduction. The 2D NiPc-Ni(NH)$_4$ showed good electrical conductivity enabled by the d-π conjugation between the nickel node and the planar Ni-phthalocyanine building block. Thus, the NiPc-Ni(NH)$_4$ nanosheets with highly exposed active sites exhibited a high CO Faradaic efficiency of 96.4% at −0.7 V and large CO partial current density of 24.8 mA cm^{-2} at −1.1 V, in excess of those previously reported for all the 2D MOF catalysts examined in H-cell. Moreover, the fully conjugated NiPc-Ni(NH)$_4$ could maintain its activity under continuous electrocatalysis test for 10 h. The combination of contrast experiment and DFT calculations revealed that the NiPc motifs are the catalytically active sites. This work sheds light on the excellent electrocatalytic behavior of intrinsically conductive 2D MOFs and provides a promising design direction for future enhancement of the activity of electrocatalyst.

Acknowledgements The work was supported by the National Key Research and Development Program of China (2018YFA0208600, 2018YFA0704502), the National Natural Science Foundation of China (21871263, 22071245, 21671188, 22033008), Strategic Priority Research Program of the Chinese Academy of Sciences (XDB20000000) and the Youth Innovation Promotion Association, CAS (Y201850). The authors thank the beamline BL14W1 station for XAS measurements at the Shanghai Synchrotron Radiation Facility, China. The authors thank Associate Prof. Mei-Rong Ke in Fuzhou University and Prof. Vefa Ahsen in Gebze Institute of Technology for guiding the synthesis of NiPc-(NHTs)$_8$.

Conflict of interest The authors declare no conflict of interest.

Supporting information The supporting information is available online at http://chem.scichina.com and http://link.springer.com/journal/11426. The supporting materials are published as submitted, without typesetting or editing. The responsibility for scientific accuracy and content remains entirely with the authors.

1 Gattuso JP, Magnan A, Billé R, Cheung WWL, Howes EL, Joos F, Allemand D, Bopp L, Cooley SR, Eakin CM, Hoegh-Guldberg O, Kelly RP, Pörtner HO, Rogers AD, Baxter JM, Laffoley D, Osborn D, Rankovic A, Rochette J, Sumaila UR, Treyer S, Turley C. *Science*, 2015, 349: aac4722
2 Wu Q, Xie RK, Mao MJ, Chai GL, Yi JD, Zhao SS, Huang YB, Cao R. *ACS Energy Lett*, 2020, 5: 1005–1012
3 He C, Chen S, Long R, Song L, Xiong Y. *Sci China Chem*, 2020, 63: 1721–1726
4 Zhang MD, Si DH, Yi JD, Zhao SS, Huang YB, Cao R. *Small*, 2020, 16: 2005254
5 Tan X, Sun X, Han B. *Natl Sci Rev*, 2021, nwab022
6 Wu Q, Mao MJ, Wu QJ, Liang J, Huang YB, Cao R. *Small*, 2021, 17: 2004933
7 Hou Y, Huang YB, Liang YL, Chai GL, Yi JD, Zhang T, Zang KT, Luo J, Xu R, Lin H, Zhang SY, Wang HM, Cao R. *CCS Chem*, 2019, 1: 384–395
8 Zheng T, Jiang K, Wang H. *Adv Mater*, 2018, 30: 1802066
9 Sun Y, Cai X, Hu W, Liu X, Zhu Y. *Sci China Chem*, 2020, 64: 1065–1075
10 Zhu W, Zhang L, Yang P, Hu C, Luo Z, Chang X, Zhao ZJ, Gong J. *Angew Chem Int Ed*, 2018, 57: 11544–11548
11 Ren X, Liu S, Li H, Ding J, Liu L, Kuang Z, Li L, Yang H, Bai F, Huang Y, Zhang T, Liu B. *Sci China Chem*, 2020, 63: 1727–1733
12 Li M, Wang H, Luo W, Sherrell PC, Chen J, Yang J. *Adv Mater*, 2020, 32: 2001848
13 Wu Q, Liang J, Xie ZL, Huang YB, Cao R. *ACS Mater Lett*, 2021, 3: 454–461
14 Kramer WW, McCrory CCL. *Chem Sci*, 2016, 7: 2506–2515
15 Cheng Y, Veder JP, Thomsen L, Zhao S, Saunders M, Demichelis R, Liu C, De Marco R, Jiang SP. *J Mater Chem A*, 2018, 6: 1370–1375
16 Zhang K, Liang Z, Zou R. *Sci China Chem*, 2020, 63: 7–10
17 Morozan A, Jaouen F. *Energy Environ Sci*, 2012, 5: 9269–9290
18 Schneemann A, Bon V, Schwedler I, Senkovska I, Kaskel S, Fischer RA. *Chem Soc Rev*, 2014, 43: 6062–6096
19 Diercks CS, Liu Y, Cordova KE, Yaghi OM. *Nat Mater*, 2018, 17: 301–307
20 Ban Y, Cao N, Yang W. *Research*, 2020, 2020: 1583451
21 Meng DL, Chen CH, Yi JD, Wu Q, Liang J, Huang YB, Cao R. *Research*, 2019, 2019: 1768595
22 Guo Y, Shi W, Yang H, He Q, Zeng Z, Ye JY, He X, Huang R, Wang C, Lin W. *J Am Chem Soc*, 2019, 141: 17875–17883

23 Ye L, Liu J, Gao Y, Gong C, Addicoat M, Heine T, Wöll C, Sun L. *J Mater Chem A*, 2016, 4: 15320–15326
24 Hod I, Sampson MD, Deria P, Kubiak CP, Farha OK, Hupp JT. *ACS Catal*, 2015, 5: 6302–6309
25 Xiong W, Li H, You H, Cao M, Cao R. *Natl Sci Rev*, 2020, 7: 609–619
26 Xie LS, Skorupskii G, Dincă M. *Chem Rev*, 2020, 120: 8536–8580
27 Matheu R, Gutierrez-Puebla E, Monge MÁ, Diercks CS, Kang J, Prévot MS, Pei X, Hanikel N, Zhang B, Yang P, Yaghi OM. *J Am Chem Soc*, 2019, 141: 17081–17085
28 Stassen I, Dou JH, Hendon C, Dincă M. *ACS Cent Sci*, 2019, 5: 1425–1431
29 Yi JD, Xie R, Xie ZL, Chai GL, Liu TF, Chen RP, Huang YB, Cao R. *Angew Chem Int Ed*, 2020, 59: 23641–23648
30 Zhong H, Ghorbani-Asl M, Ly KH, Zhang J, Ge J, Wang M, Liao Z, Makarov D, Zschech E, Brunner E, Weidinger IM, Zhang J, Krasheninnikov AV, Kaskel S, Dong R, Feng X. *Nat Commun*, 2020, 11: 1409
31 Zhang XD, Hou SZ, Wu JX, Gu ZY. *Chem Eur J*, 2020, 26: 1604–1611
32 Sheberla D, Sun L, Blood-Forsythe MA, Er S, Wade CR, Brozek CK, Aspuru-Guzik A, Dincă M. *J Am Chem Soc*, 2014, 136: 8859–8862
33 Jia H, Yao Y, Zhao J, Gao Y, Luo Z, Du P. *J Mater Chem A*, 2018, 6: 1188–1195
34 Lian Y, Yang W, Zhang C, Sun H, Deng Z, Xu W, Song L, Ouyang Z, Wang Z, Guo J, Peng Y. *Angew Chem Int Ed*, 2020, 59: 286–294
35 Chen T, Dou JH, Yang L, Sun C, Libretto NJ, Skorupskii G, Miller JT, Dincă M. *J Am Chem Soc*, 2020, 142: 12367–12373
36 Hu JX, Jiang XF, Ma YJ, Liu XR, Ge BD, Wang AN, Wei Q, Wang GM. *Sci China Chem*, 2021, 64: 432–438
37 Fei H, Dong J, Arellano-Jiménez MJ, Ye G, Dong Kim N, Samuel ELG, Peng Z, Zhu Z, Qin F, Bao J, Yacaman MJ, Ajayan PM, Chen D, Tour JM. *Nat Commun*, 2015, 6: 8668
38 Han Y, Wang YG, Chen W, Xu R, Zheng L, Zhang J, Luo J, Shen RA, Zhu Y, Cheong WC, Chen C, Peng Q, Wang D, Li Y. *J Am Chem Soc*, 2017, 139: 17269–17272
39 Wang J, Li N, Xu Y, Pang H. *Chem Eur J*, 2020, 26: 6402–6422
40 Peng Y, Yang W. *Sci China Chem*, 2019, 62: 1561–1575
41 Kornienko N, Zhao Y, Kley CS, Zhu C, Kim D, Lin S, Chang CJ, Yaghi OM, Yang P. *J Am Chem Soc*, 2015, 137: 14129–14135
42 Guntern YT, Pankhurst JR, Vávra J, Mensi M, Mantella V, Schouwink P, Buonsanti R. *Angew Chem Int Ed*, 2019, 58: 12632–12639
43 Mao F, Jin YH, Liu PF, Yang P, Zhang L, Chen L, Cao XM, Gu J, Yang HG. *J Mater Chem A*, 2019, 7: 23055–23063
44 Dong BX, Qian SL, Bu FY, Wu YC, Feng LG, Teng YL, Liu WL, Li ZW. *ACS Appl Energy Mater*, 2018, 1: 4662–4669
45 Wang Y, Hou P, Wang Z, Kang P. *ChemPhysChem*, 2017, 18: 3142–3147
46 Jiang X, Li H, Xiao J, Gao D, Si R, Yang F, Li Y, Wang G, Bao X. *Nano Energy*, 2018, 52: 345–350
47 Yang Z, Zhang X, Long C, Yan S, Shi Y, Han J, Zhang J, An P, Chang L, Tang Z. *CrystEngComm*, 2020, 22: 1619–1624
48 Zhu S, Li T, Cai WB, Shao M. *ACS Energy Lett*, 2019, 4: 682–689
49 Zhang MD, Yi JD, Huang YB, Cao R. *Chin J Struct Chem*, 2021, doi: 10.14102/j.cnki.0254-5861.2011-3118
50 Wang L, Chen W, Zhang D, Du Y, Amal R, Qiao S, Wu J, Yin Z. *Chem Soc Rev*, 2019, 48: 5310–5349